



Combined X-ray diffraction and absorption tomography using a conical shell beam

A. SHEVCHUK,¹ J. P. O. EVANS,^{1,*} A. J. DICKEN,¹ F. ELARNAUT,¹ D. DOWNES,¹ S. X. GODBER,² AND K. D. ROGERS³

¹Imaging Science Group, Rosalind Franklin Building, Nottingham Trent University, Nottingham, UK

²Halo X-ray Technologies, BioCity, Nottingham, UK

³Cranfield Forensic Institute, Cranfield University, Shrivvenham, Swindon, UK

*paul.evans@ntu.ac.uk

Abstract: We combine diffraction and absorption tomography by raster scanning samples through a hollow cone of pseudo monochromatic X-rays with a mean energy of 58.4 keV. A single image intensifier takes 90x90 (x,y) snapshots during the scan. We demonstrate a proof-of-principle of our technique using a heterogeneous three-dimensional (x,y,z) phantom (90x90x170 mm³) comprised of different material phases, i.e., copper and sodium chlorate. Each snapshot enables the simultaneous measurement of absorption contrast and diffracted flux. The axial resolution was ~ 1 mm along the (x,y) orthogonal scan directions and ~ 7 mm along the z -axis. The tomosynthesis of diffracted flux measurements enable the calculation of d -spacing values with ~ 0.1 Å full width at half maximum (FWHM) at ~ 2 Å. Thus the identified materials may be color-coded in the absorption optical sections. Characterization of specific material phases is of particular interest in security screening for the identification of narcotics and a wide range of homemade explosives concealed within complex “everyday objects.” Other potential application areas include process control and biological imaging.

© 2019 Optical Society of America under the terms of the OSA Open Access Publishing Agreement

1. Introduction

Radiographic imaging and the structural analysis of materials using X-rays developed disparately soon after the discovery of X-rays in 1895 [1]. The former has evolved from simple planar imaging into sophisticated tomographic methods [2,3], while the latter formed the basis of X-ray crystallography. Each approach demands quite different spatiotemporal collection and sensing requirements [4,5]. In general, incident X-rays composing a spatial image propagate along a linear path from the source to the detector and do not interact with the materials under inspection. However, the spectroscopic analysis of the transmitted X-rays may provide some useful materials discrimination information [6]. Ultimately, such approaches are limited fundamentally and cannot provide structural or ‘molecular resolution’ analysis. In contrast, determination of the atomic and molecular structure of crystalline/polycrystalline materials requires analysis of coherently scattered or diffracted X-rays from a sample. The relatively low energy of the interrogating radiation used in laboratory X-ray diffraction (XRD) limits penetration into the sample to near the incident surface. Significantly higher X-ray energies are required (i.e. an order of magnitude increase in photon energy over the legacy 8 keV Cu K α [7]) for transmission mode diffraction for highly absorbing and or extended thickness samples [7–9]. Conventional fan beam tomography has provided diffracted flux measurements [5,9–11] to demonstrate spatially-resolved material specific profiles. Novel compressive tomography promises further reductions in scan times and exposure [12–14]. The common problem confronting all volumetric XRD scanning/imaging methods is the production and measurement of sufficient diffracted flux or signal photons to provide the desired scan speed at application dependent energies. These considerations are a significant hurdle in the ongoing development of practical high-energy XRD scanning technology. These challenges appear whenever seeking to combine

transmission mode XRD with transmission imaging. The many fields that would benefit from combining spatial imaging with structural characterization include material science, security screening and medicine.

The driver for the work concerns the security screening of air passenger luggage. It is routine to employ absorption imaging to help detect shape-based threats such as guns, knives and sharps, buried within a stream-of-objects. Security personnel have around 5 seconds to detect such threats using standard X-ray transmission systems, where false detections require additional scanning and hand searching. Critically, wide ranges of plastic, liquid and homemade explosives (HMEs) present shape-variant threats that also require accurate materials information. The dual-energy X-ray materials discrimination method has been widely applied in a range of imaging formats including; single view or 2D [15], dual (orthogonal) view [15], binocular stereoscopic [16], and multiview [17,18]. The relatively recent deployment of CT scanners in security screening enables the computation of average atomic number and density. This additional data improves the probability of the detection of threats and reduces false alarm rates. However, the spectral measurement and analysis of transmitted X-rays is ultimately limited in terms of materials resolution. To enhance the sensitivity and specificity requires an orthogonal probe [6,19]. If depth-resolved absorption and diffraction imaging [12,20] were combined successfully in a compact and cost-effective technology, then it could be deployed to increase the throughput of carry-on and checked luggage at international travel hubs. It is, therefore, a desirable proposition to combine both the collection and analysis of diffracted flux with absorption imaging to potentially reduce false-alarm rates. This technological development would be a significant and disruptive advance for material specific security screening applications.

In this paper, we report for the first time the combined application of tomosynthesis to absorption image contrast and XRD signals collected simultaneously via a single scanning hollow beam probe and planar detector. We build directly upon our prior work, which has developed conical shell absorption tomography [21] and independently, conical shell XRD tomography [22]. In our approach, the sample acts as a ‘diffractive lens’ to focus coherent scatter onto a detector placed within the central dark area and surrounded by the primary beam. To demonstrate our method, we simultaneously scan a pair of samples with similar absorption contrast but different XRD profiles. We employ conventional XRD characterization to identify the samples and enable material specific color-coding in the constructed images. The reported status of the technique is that of a proof-of-principle experiment.

The organization of our paper is as follows. Section 2 presents the methods including the theory background; our combined imaging technique and describes the experiment conditions. Section 3 presents our experiment results and associated discussion. Section 4 summarizes our conclusions, discusses the implications of our findings and the future direction of the work

2. Methods

2.1. Theory background

Our group has previously reported the use of hollow conical probes, collectively termed focal construct geometry (FCG) [23], as an alternative to pencil or linear beams employed conventionally in the lab-based XRD systems. The FCG method produces relatively bright material specific patterns in the diffracted flux, termed caustics [24]. The high-intensity caustic patterns may be used to reduce exposure times [22,25] and increase scan speed in comparison to competing techniques. Development of FCG in angular dispersive mode has been investigated using various scanning regimes, including sample-to-source [25,26] and detector-to-source translation [27]. In angular dispersive mode a pseudo monochromatic X-ray beam is applied via balanced filtering [24]. We have also investigated a stationary energy dispersive FCG mode, where polychromatic focal spots [26] were measured on a centrally

positioned energy resolving point detector [28]. The caustics can be measured to discriminate between various materials, including structurally complex, non-ideal samples at both low and high energies [24,27,29,30], where they benefit from the relatively extended gauge volumes. FCG is also capable of classifying liquid samples [29], which combined with its ability to obtain diffraction signatures in transmission using high X-ray energies from both polycrystalline and semi-crystalline materials make it a compelling technique for security screening applications. The fast and accurate identification of commercial and homemade explosives (HMEs) is a critical consideration in this problem space. Our paper is a natural extension of this prior body of work and in particular our work on FCG transmission tomography [21] and diffraction tomography [22]. It reports the first demonstration of combined XRD and absorption FCG tomography using a single conical shell beam and detection surface.

2.2. Combined imaging technique

A sample is raster scanned (x,y) through a conical shell X-ray beam. Bright field (absorption contrast) signals and dark field (diffracted flux) signals are incident simultaneously on a flat spatially resolving detection plane oriented normally with respect to the primary beam; see Fig. 1(a). The concurrent measurement of diffracted flux and absorption contrast is implemented through the acquisition of a stream of discrete planar snapshots. The (x,y) position of each snapshot during the scan may be described via a grid of relative X-ray focus positions, see Fig. 1(b).

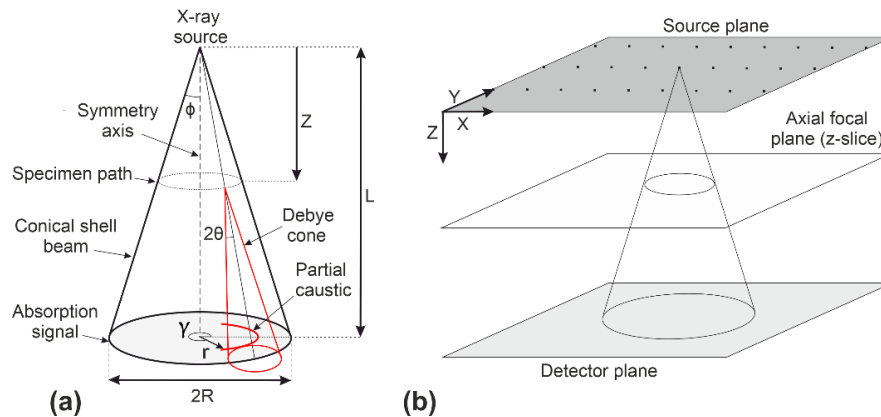


Fig. 1. (a) A conical shell X-ray beam with a beam half-opening angle $\phi \sim 3.92^\circ$ produces a circular footprint upon a planar detection surface at a distance L from the X-ray focus. A Debye cone originating along a specimen path at distance z from the X-ray focus contributes to the formation of a caustic in the diffracted flux. (b) Raster scanning a phantom through the shell beam is geometrically equivalent to scanning the beam through a stationary phantom. The relative (x,y) position of a sequence of snapshots forms a coplanar grid of X-ray focus positions. The axial focal plane positions of the reconstructed optical sections or z -slices are parallel with the X-ray focus plane and the detector plane.

Each snapshot comprises a primary beam footprint together with caustics [22] in the diffracted flux within the central detection area. The measurements of absorption contrast at fixed polar coordinate positions R on each different transmission absorption ring, collected by a fixed detector pixel, may be composited to form oblique projections [21]. The maximum total number of different oblique projections is equal to the total number of detector pixels or sampling positions around the primary beam footprint. Whereas the total number of axial (x,y) pixels composing an oblique projection is equal to the total number of coplanar X-ray focus grid positions or snapshots i.e. one pixel for each different oblique projection is acquired per grid position. The minimum angular separation between each composite oblique

projection (equivalent to a rotation about the symmetry axis) is parametrized by the increment in polar angle $\delta\gamma$ separating adjacent ‘ring’ detector pixels. To effect an axial focal plane normal to the z -axis each oblique image requires relatively shifting along the direction of the polar angle γ specified by the relevant detector pixel, see Fig. 1(a). In other words, voxels are reconstructed from measurements acquired along different interrogating ray paths at different scan times/relative positions during the scan. This process enables the “diffractive lensing” reported with staring beams and extended samples [23] to be recreated on a voxel-by-voxel basis by raster scanning/tomosynthesis [22]. A zero shift and a maximum shift identify the two (hypothetical) axial planes that bound the theoretical inspection volume at the point source and the detector surface, respectively. The pixel shift is linearly proportional to distance along the z -axis due to the reconstructed oblique interrogating ray geometry. For example, the nominal separation between two neighboring focal plane positions is given by $\delta z = \delta p / 2 \tan \phi$, where δp is the minimum detectable increment in circular parallax, which is equal to the axial step or scan distance $\delta x = \delta y = \delta p$ between adjacent detector/beam snapshot positions. The resultant ray geometry is equivalent to an inclined parallel beam incident upon a rotating phantom or a rotating source of parallel X-rays about a stationary phantom. This aspect is counterintuitive as only linear motion is required during image acquisition [21]. In an analog of this method [22], the measurement of caustic paths that intersect a polar direction γ but with different polar magnitudes r , each form a separate oblique image corresponding to a d-spacing present in the sample given by

$$d = \frac{\lambda}{2 \sin \left(\frac{1}{2} \left\{ \phi + \tan^{-1} \left[\left(\frac{R \pm r}{L - z} \right) - \tan \phi \right] \right\} \right)} \quad (1)$$

where the wavelength λ is given via the Planck-Einstein relation and the tomosynthesis angle 2ϕ is equal to the conical shell beam opening angle. The sign of the polar magnitude r provides the direction of the radial pixel shift to effect a focal plane image [22]. This parametrization is necessary as a caustic of a given radius r can be produced for different combinations of axial position z and diffraction angle 2θ , which include the possibility of Debye cones crossing the symmetry axis of the primary beam e.g. cones originating at γ and $(\gamma + \pi)$ will intersect in front of the detector [22]. All such combinations including the ‘crossover’ condition are disambiguated via shift-and-add tomosynthesis, enabling unequivocal calculation of d-spacing from Eq. (1). Thus, each optical section or z -slice records diffracted flux satisfying Bragg’s condition for a single d-spacing value. Consequently, both diffraction optical sections and absorption sections through a sample are congruent and exhibit one-to-one spatial mapping. To study each modality independently the reader is directed to the detailed theory and experimental results previously reported [21–24].

2.3. Experiment conditions

The experiment rig employed a Hamamatsu microfocus X-ray source (Model L9181-02) with tungsten target and focal spot size of 40 μm , and an accelerating voltage and current of 130 kV and 300 μA , respectively. A conical shell beam was produced with the aid of a bespoke tungsten collimator with a mean half-opening angle $\phi = 3.92^\circ$ where $\phi_{\text{max}} = 3.97^\circ$ and $\phi_{\text{min}} = 3.87^\circ$, which corresponds to a shell thickness of ~ 0.2 mm at the output of the ring collimator and ~ 1 mm at the input face of the image intensifier. Following the source, 0.1 mm thick thulium (K-edge 59.3896 keV) and erbium (K-edge 57.4855) rare earth metal filters are mounted on a motorized filter wheel (Thorlabs FW102C-PC2 REV-D). A Hamamatsu X-ray image intensifier (model C7336-10H) with a 4-inch diameter (~ 102 mm), 0.5 mm thick aluminum input window and CsI input phosphor screen was coupled optically to an 8.26×6.6 mm² area, 1280×1024 pixel, 12-bit low noise CCD camera (Bigeye G-132B). The collection of scattered X-ray photons occurred over a 60 mm diameter detection window.

Figure 2 shows the configuration in detail. The absorption contrast measurements were recorded around the annular primary beam footprint with a mean diameter $R = 41.1$ mm. To ensure that the relative intensities of the incident primary flux and diffracted flux were within the quantization window of the image intensifier a 3 mm thick ring of lead attenuated the primary beam. The image exposure time was 10 seconds and two images, one per filter, acquired per scan position. The detector positioned at $L = 600$ mm from the X-ray focus supported a d-spacing range of 1.22 \AA to 10.58 \AA . This d-spacing range provides potential discrimination of materials such as drugs ($1.7\text{-}3 \text{ \AA}$) [31], metals ($0.5\text{-}2.5 \text{ \AA}$) and organics ($2\text{-}10 \text{ \AA}$) [32]. Diffracted flux measurements from samples were obtained using a primary beam pseudo monochromatized around the tungsten $K\alpha$ line, 0.209 \AA ($\sim 59.3 \text{ keV}$) where the subtraction of the two filtered images, i.e. Tm-Er provided an effective 1.9 keV energy window with a mean energy of 58.4 keV .

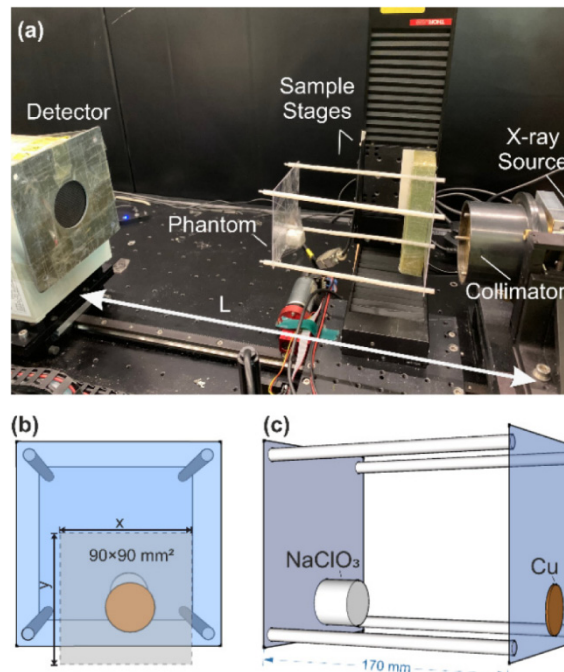


Fig. 2. (a) Photograph of the FCG experiment setup with the system components highlighted. (b) Plan view graphic of the phantom showing the outline of the raster scanned region providing a $90 \times 90 \times 170 \text{ mm}^3$ inspection volume (via the projection of the of X-ray focus positions). (c) Side-view graphic showing relative positions of the two samples. Note that the oblique (parallel) X-ray views generated by our method do not exhibit a change in magnification as a function of range (z -axis) as illustrated by the ‘point projection’ graphics.

The phantom consisted of two samples each with different crystallographic properties, namely a copper disk and a sodium chlorate sample with cylindrical shape see Table 1. The latter material is an explosive precursor regulated under the EPP license in the UK. The different thicknesses of the samples provide similar gray levels in the absorption X-ray images.

Table 1. Details of the sample materials used in the phantom.

Samples	Thickness/Diameter (mm)	Crystallite character	ICDD card number
Copper	0.8/19	Preferred orientation	01-085-1326
Sodium chlorate	18/17	Large grain size	00-005-0610

The phantom was raster scanned using (x,y) linear translation stages (Thorlabs NRT150 with a minimum repeatable incremental movement of 4 μm) to acquire $90 \times 90 = 8100$ snapshots with axial step sizes $\delta x = \delta y = 1 \text{ mm}$ over the phantom volume of $\sim 90 \times 90 \times 170 \text{ mm}^3$. To match an optical section in absorption space with corresponding material signatures in diffraction space required the production of a set of optical sections parallel with the detection plane; one per d-spacing at a given axial focal plane position. The spatial registration of the diffracted flux measurements attributed to the same coordinate position enables the calculation of a 1D-diffractogram per voxel. A Savitsky Golay filter (MATLAB (R2018a)) was applied to the diffractograms. Reference diffraction profiles from both copper and sodium chlorate were obtained from a prior high-energy FCT experiment (example [23]) to enable comparison with the 'unknown' material profiles being performed via the Pearson correlation coefficient (PCC) (MATLAB (R2018a) function 'corr' [33–36]). The PCC threshold value was determined by using the receiver operating characteristic (ROC) curve with criteria of sensitivity ≥ 0.9 and specificity ≥ 0.9 . Based on the available materials and ROC criteria, it was determined valid diffraction profile matches have a PCC value > 0.58 . This threshold was applied to all pixels composing the reconstructed image. According to our theory [21,22] valid material matches should occur at coincident axial positions for both diffraction and absorption optical sections throughout the samples.

3. Results and discussion

Constructed images through the copper sample are illustrated in Fig. 3 together with the resultant 1D-diffraction profiles. Similarly, Fig. 4 shows the constructed images through the sodium chlorate sample and the associated diffraction profiles. As previously discussed, PCC analysis on a voxel-by-voxel basis was applied using 1D-reference patterns to the optical sections. Well-matched voxels and by extension optical sections were observed at calculated axial positions of 164 mm and 313 mm i.e. consistent with manual measurement of the sample positions. As predicted by our theory, where the same radial shift values (see Figs. 3 and 4) are applied to both XRD and absorption the result is in-focus planes with one-to-one spatial (x,y,z) correspondence. This result is a function of the primary beam geometry i.e. encoding of position is nominally independent of the diffraction angle. The in-plane spatial resolution of the optical sections was $\sim 1 \text{ mm}$, as predicted by the axial step sizes $\delta x = \delta y = 1 \text{ mm}$. The thickness of the optical sections can be approximated as $\delta z \sim 7 \text{ mm}$ (see Section 2.2) and is consistent with observed results. These findings establish that the spatial resolution in each of the (x,y,z) imaging axes are nominally independent of the z-slice position because the reconstructed parameters are a function of oblique (parallel) projections i.e. magnification from object to image space is constant. Thus, the spatial resolution is independent of the probing beam diameter at the z-slice under consideration. For example, the 17 mm diameter sodium chlorate sample ($z = 313 \text{ mm}$) was measured using $\sim 43 \text{ mm}$ beam diameter while the 19 mm diameter copper sample ($z = 164 \text{ mm}$) was measured using $\sim 23 \text{ mm}$ beam diameter. This aspect of our technique exploits the 'virtual convergence' of the physical beam geometry using shift-and-add tomosynthesis [21]. It has been stated previously and the results presented here reinforce the hypothesis that the resultant multidirectional illumination of a specimen improves the particle statistics. Crystallographic parameters including texture and grain size are expected to influence the ability to detect minimum amounts of a material. However, the systematic study of polycrystalline structure on spatial resolution is beyond the scope of this paper. Although, we are able to report that inherently weak diffraction signals appear to be more accurately focused via 'parallel' absorption focusing. It was also observed that out of focus Bragg peaks 'bleed' into adjacent optical sections in the experiment results. This finding is consistent with the axial blurring encountered in all limited angle tomography of extended objects. Several different steps have been taken to reduce the impact of bleed on the material signature analysis; including increasing the PCC match threshold and ensuring comparison over the same 2θ range with the reference/target material.

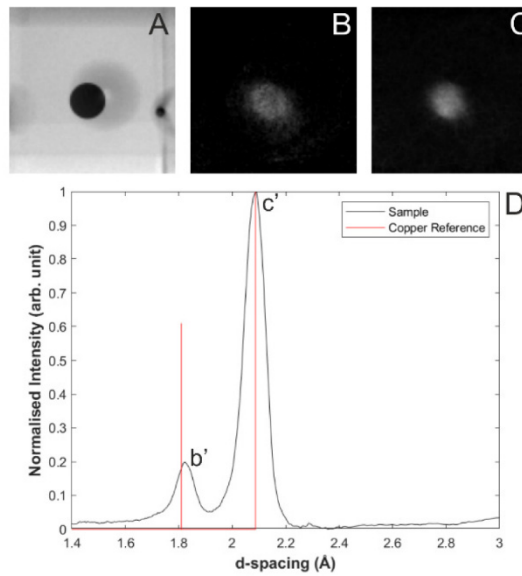


Fig. 3. (A) Absorption contrast optical section through a copper disk at 164 mm along the z -axis (including the out-of-focus artifact from the sodium chlorate sample). (B) Spatially corresponding diffraction (single d -spacing) optical section for the (200) Bragg peak of copper at 1.82 Å and (C) the optical section for the (111) Bragg peak at 2.08 Å. The 1D-diffraction profile for the material is shown in (D) where the Bragg peaks, b' and c' refer to the uppercase labeled optical sections, respectively. From the above it was estimated that the FWHM for b' and c' is 0.1 Å and 0.08 Å, respectively.

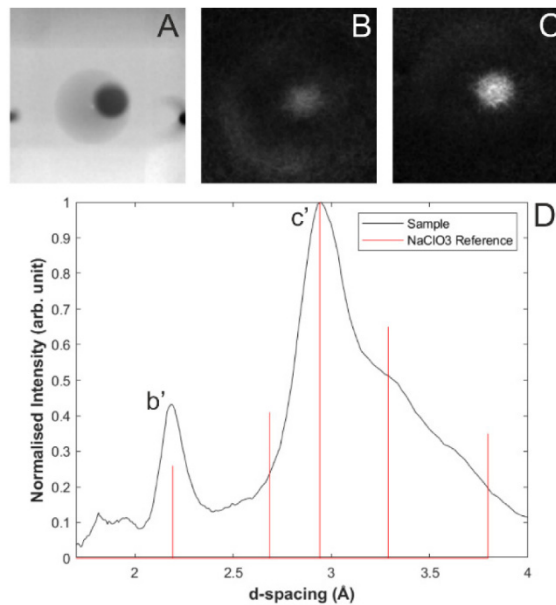


Fig. 4. (A) Absorption optical section through a sodium chlorate sample at 313 mm along the z -axis (including the out-of-focus artifact from the copper sample). (B) Spatially corresponding diffraction optical section (single d -spacing) for a the (221) Bragg peak for sodium chlorate at 2.18 Å and (C) showing the optical section for the (210) Bragg peak at 2.95 Å. The 1D-diffraction profile for the material is shown in (D) where the Bragg peaks, b' and c' refer to the uppercase labeled optical sections, respectively.

The matches were then used to construct a voxelated image, where each voxel is assigned a material identity. Material specific signatures can then be color coded in the corresponding absorption section. Figure 5 shows the output of the combined system when the two-layered phantom was analyzed. Here the presence, location, and identity of the material under inspection are fused.

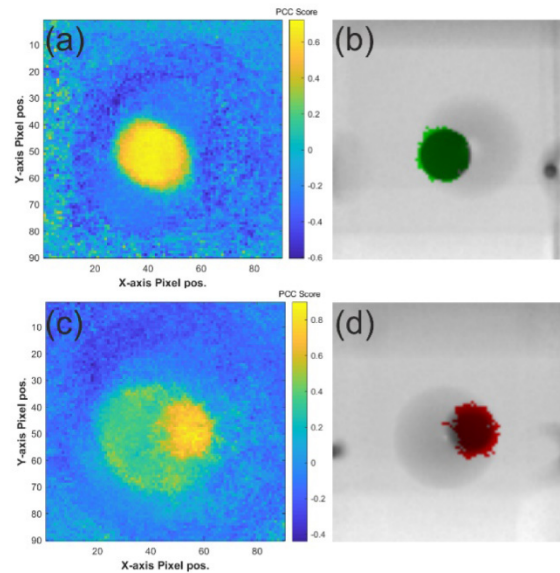


Fig. 5. (a) PCC heat map of a match result per pixel for the diffraction optical sections through a copper disk (164 mm along the z -axis). (b) Absorption optical section of a copper sample color-coded (green) via analysis of the diffraction optical sections. (c) PCC heat map of a match result per pixel for the diffraction optical sections through the sodium chlorate sample (313 mm along the z -axis). (d) Absorption optical section of the sodium chlorate sample color-coded (red) via analysis of the diffraction optical sections.

The PCC heat maps of the reconstructed ‘Bragg maxima’ identify the materials of interest in the diffraction z -slices as shown in Figs. 5(a) and (c). The spatial congruence of the absorption and diffraction z -slices (through the samples) enabled the mapping of the identified material phase to be mapped directly onto the corresponding absorption z -slices, as shown in Figs. 5(b) and (d). In our experiment, a green color indicates copper and a red color indicates sodium chlorate, an explosive precursor. As previously shown, the method performs robustly in the presence of polycrystalline and semi-polycrystalline textured materials [24,28].

4. Conclusions and future work

We report a proof-of-principle demonstration of combined XRD and absorption tomography employing a single hollow beam probe optically coupled to a detection surface. No a priori knowledge of the sample position or tight collimation of the scattered X-ray flux is required. The single beam and detector setup enable spatially correlated optical sections produced by two orthogonal modalities to support and inform shape-based and or material specific inspection processes. This approach is a natural addition to the ongoing development of a body of work collectively exploiting focal construct geometry (FCG) [24].

A fundamental requirement for both transmission imaging and XRD is that sufficient X-ray flux propagates through the objects under inspection for meaningful analysis. The design of the primary beam topology is a function of operational energy range. A reduction in the opening angle of the probing beam to accommodate the increasingly forward direction of high-energy diffracted flux results in a concomitant reduction in axial resolution. The

resultant thicker optical sections and increased angular uncertainty produces peak broadening in the resultant 1D diffractograms. The reduction in the width of the primary collimation slit to produce a thinner conical shell can mitigate this effect [28].

We conclude that our approach is a promising avenue for further research into the detection and characterization of threat materials hidden within a heterogeneous three-dimensional aggregate of objects. Our technique may also be applicable for mixed materials and those of lower crystallographic order e.g. nanomaterials, where the diffractograms produced may be treated analytically by conventional diffraction approaches for quantification and microstructural analyses. Future work will investigate replacing the pseudo monochromatic detection arrangement with a pixelated energy-resolving detector optically coupled to a polychromatic beam. For example, we have previously reported energy-dispersive XRD using hollow beam probes with sub-second acquisition times of 0.5 s equating to 0.15 mAs [28] and depth-resolved snapshot probes operating at 0.3 mAs [37]. In addition, sporadic sampling [38] emulates the sparse firing of an array of hollow beam emission points to provide a potential 90% reduction in snapshot/X-ray focus grid positions. Given the scalability of our methods in both scan space and X-ray energy, we hypothesize that a realistic research objective is the translation of objects under inspection through a multisource inspection system of the order of 0.2 m/s. Ultimately, we are pursuing a compact and cost-effective technology to reduce significantly false alarm rates in the security screening of luggage. Other application areas include diagnostic imaging for bone quality [39,40] and process control.

Funding

Department of Homeland Security (DHS), Science and Technology Directorate, Homeland Security Advanced Research Projects Agency, Explosives Division through the Advanced X-ray Material Discrimination Program (HSHQDC-15-CB0036); Royal Society and Wolfson Foundation, under a Royal Society Wolfson Fellowship and grant RSWF\R1\180012.

References

1. W. C. Röntgen, "On a new kind of rays," *Science* **3**(59), 227–231 (1896).
2. T. Gomi, H. Hirano, and T. Umeda, "Evaluation of the X-ray digital linear tomosynthesis reconstruction processing method for metal artifact reduction," *Comput. Med. Imaging Graph.* **33**(4), 267–274 (2009).
3. C. B. Reid, M. M. Betcke, D. Chana, and R. D. Speller, "The development of a pseudo-3D imaging system (tomosynthesis) for security screening of passenger baggage," *Nucl. Instrum. Methods Phys. Res. A* **652**(1), 108–111 (2011).
4. G. Harding, H. Fleckenstein, D. Kosciesza, S. Olesinski, H. Strecker, T. Theedt, and G. Zienert, "X-ray diffraction imaging with the Multiple Inverse Fan Beam topology: principles, performance and potential for security screening," *Appl. Radiat. Isot.* **70**(7), 1228–1237 (2012).
5. A. Vamvakeros, S. D. M. Jacques, M. Di Michiel, P. Senecal, V. Middelkoop, R. J. Cernik, and A. M. Beale, "Interlaced X-ray diffraction computed tomography," *J. Appl. Cryst.* **49**, 485–496 (2016).
6. K. Wells and D. A. Bradley, "A review of x-ray explosives detection techniques for checked baggage," *Appl. Radiat. Isot.* **70**(8), 1729–1746 (2012).
7. G. Harding and A. Harding, "X-ray diffraction imaging for explosives detection," in *Counterterrorist Detection Techniques of Explosives*, J. Yinon, ed. (Elsevier B.V., 2007), pp. 199–223.
8. D. O'Flynn, C. Crews, I. Drakos, C. Christodoulou, M. D. Wilson, M. C. Veale, P. Seller, and R. D. Speller, "Materials identification using a small-scale pixelated x-ray diffraction system," *J. Phys. D Appl. Phys.* **49**(17), 1–10 (2016).
9. Z. Zhu, A. Katsevich, A. J. Kapadia, J. A. Greenberg, and S. Pang, "X-ray diffraction tomography with limited projection information," *Sci. Rep.* **8**(1), 522 (2018).
10. A. H. Khan and R. A. Chaudhuri, "Fan-beam geometry based inversion algorithm in computed tomography (CT) for imaging of composite materials," *Compos. Struct.* **110**, 297–304 (2014).
11. K. P. MacCabe, A. D. Holmgren, M. P. Tornai, and D. J. Brady, "Snapshot 2D tomography via coded aperture x-ray scatter imaging," *Appl. Opt.* **52**(19), 4582–4589 (2013).
12. J. Greenberg, K. Krishnamurthy, and D. Brady, "Compressive single-pixel snapshot x-ray diffraction imaging," *Opt. Lett.* **39**(1), 111–114 (2014).
13. Y. Kaganovsky, D. Li, A. Holmgren, H. Jeon, K. P. MacCabe, D. G. Polite, J. A. O'Sullivan, L. Carin, and D. J. Brady, "Compressed sampling strategies for tomography," *J. Opt. Soc. Am. A* **31**(7), 1369–1394 (2014).

14. J. A. Greenberg and D. J. Brady, "Structured illumination for compressive x-ray diffraction tomography," *Proc. SPIE* **9020**, 902001 (2014).
15. M. Marshall and J. C. Oxley, *Aspects of Explosives Detection* (Elsevier B.V., 2009).
16. J. P. O. Evans, "Kinetic depth effect X-ray (KDEX) imaging for security screening," in *International Conference on Visual Information Engineering (VIE, 2003)*, pp. 69–72.
17. Z. Ying, R. Naidu, and C. R. Crawford, "Dual energy computed tomography for explosive detection," *J. XRay Sci. Technol.* **14**, 235–256 (2006).
18. R. K. Kaza, J. F. Platt, R. H. Cohan, E. M. Caoili, M. M. Al-Hawary, and A. Wasnik, "Dual-energy CT with single- and dual-source scanners: current applications in evaluating the genitourinary tract," *Radiographics* **32**(2), 353–369 (2012).
19. S. Michel, M. Mendes, and A. Schwaninger, "Can the difficulty level reached in computer-based training predict results in x-ray image interpretation tests?" in *Proceedings of IEEE Conference on Security Technology (IEEE, 2010)*, pp. 148–154.
20. R. Moss, C. Crews, M. Wilson, and R. Speller, "miniPixD: A compact sample analysis system which combines X-ray imaging and diffraction," *J. Instrum.* **12**(02), 1–16 (2017).
21. J. P. O. Evans, S. X. Godber, F. Elarnaut, D. Downes, A. J. Dicken, and K. D. Rogers, "X-ray absorption tomography employing a conical shell beam," *Opt. Express* **24**(25), 29048–29059 (2016).
22. P. Evans, K. Rogers, A. Dicken, S. Godber, and D. Prokopiou, "X-ray diffraction tomography employing an annular beam," *Opt. Express* **22**(10), 11930–11944 (2014).
23. A. Dicken, A. Shevchuk, K. Rogers, S. Godber, and P. Evans, "High energy transmission annular beam X-ray diffraction," *Opt. Express* **23**(5), 6304–6312 (2015).
24. K. Rogers and P. Evans, "X-ray diffraction and focal construct technology," in *X-Ray Diffraction Imaging: Technology and Applications*, J. Greenberg, ed. (CRR Press, 2018).
25. K. Rogers, P. Evans, J. Rogers, J. Chan, and A. Dicken, "Focal construct geometry – a novel approach to the acquisition of diffraction data," *J. Appl. Cryst.* **43**(2), 264–268 (2010).
26. P. Evans, K. Rogers, J. Chan, J. Rogers, and A. Dicken, "High intensity x-ray diffraction in transmission mode employing an analog of Poisson's spot," *Appl. Phys. Lett.* **97**(20), 204101 (2010).
27. K. Rogers, P. Evans, D. Prokopiou, A. Dicken, S. Godber, and J. Rogers, "Fundamental parameters approach applied to focal construct geometry for x-ray diffraction," *Nucl. Instrum. Methods Phys. Res. A* **690**, 1–6 (2012).
28. A. J. Dicken, J. P. O. Evans, K. D. Rogers, C. Greenwood, S. X. Godber, D. Prokopiou, N. Stone, J. G. Clement, I. Lyburn, R. M. Martin, and P. Zioupos, "Energy-dispersive X-ray diffraction using an annular beam," *Opt. Express* **23**(10), 13443–13454 (2015).
29. D. Prokopiou, K. Rogers, P. Evans, S. Godber, and A. Dicken, "Discrimination of liquids by a focal construct X-ray diffraction geometry," *Appl. Radiat. Isot.* **77**, 160–165 (2013).
30. D. Prokopiou, K. Rogers, P. Evans, S. Godber, J. Shackel, and A. Dicken, "X-ray diffraction with novel geometry," *Nucl. Instrum. Methods Phys. Res. A* **735**, 341–348 (2014).
31. E. Cook, R. Fong, J. Horrocks, D. Wilkinson, and R. Speller, "Energy dispersive X-ray diffraction as a means to identify illicit materials: a preliminary optimisation study," *Appl. Radiat. Isot.* **65**(8), 959–967 (2007).
32. M. C. Green and L. D. Partain, "High throughput baggage scanning employing x-ray diffraction for accurate explosives detection," *Proc. SPIE* **5048**, 63–72 (2003).
33. J. Benesty, J. Chen, and Y. Huang, "On the importance of the Pearson correlation coefficient in noise reduction," in *Proceedings of IEEE Conference on Audio, Speech and Language Processing (IEEE, 2008)*, pp. 757–765.
34. A. Dicken, D. Spence, K. Rogers, D. Prokopiou, and P. Evans, "Dual conical shell illumination for volumetric high-energy X-ray diffraction imaging," *Analyst (Lond.)* **143**(20), 4849–4853 (2018).
35. N. Altman and M. Krzywinski, "Association, correlation and causation," *Nat. Methods* **12**(10), 899–900 (2015).
36. M. Puth, M. Neuhauser, and G. D. Ruxton, "Effective use of Pearson's product-moment correlation coefficient," *Anim. Behav.* **93**, 183–189 (2014).
37. A. J. Dicken, J. P. O. Evans, K. D. Rogers, D. Prokopiou, S. X. Godber, and M. Wilson, "Depth resolved snapshot energy-dispersive X-ray diffraction using a conical shell beam," *Opt. Express* **25**(18), 21321–21328 (2017).
38. F. Elarnaut, J. P. O. Evans, D. Downes, A. J. Dicken, S. X. Godber, and K. D. Rogers, "Sporadic absorption tomography using a conical shell X-ray beam," *Opt. Express* **25**(26), 33029–33042 (2017).
39. A. J. Dicken, J. P. O. Evans, K. D. Rogers, N. Stone, C. Greenwood, S. X. Godber, D. Prokopiou, J. G. Clement, I. D. Lyburn, R. M. Martin, and P. Zioupos, "X-ray diffraction from bone employing annular and semi-annular beams," *Phys. Med. Biol.* **60**(15), 5803–5812 (2015).
40. A. J. Dicken, J. P. O. Evans, K. D. Rogers, N. Stone, C. Greenwood, S. X. Godber, J. G. Clement, I. D. Lyburn, R. M. Martin, and P. Zioupos, "Classification of fracture and non-fracture groups by analysis of coherent X-ray scatter," *Sci. Rep.* **6**(1), 29011 (2016).